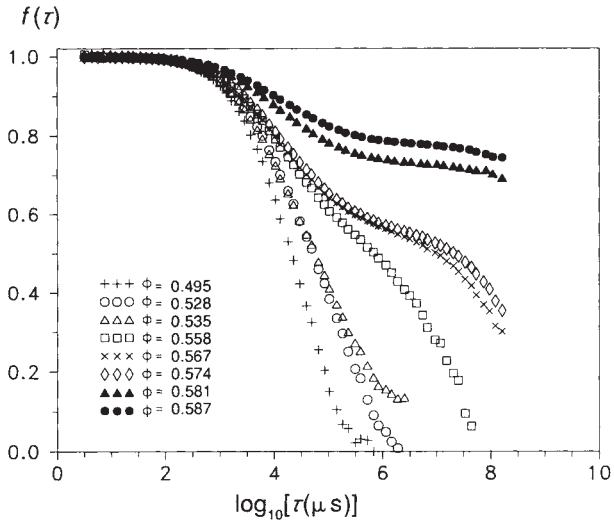

FIG. 2 Autocorrelation functions, $f(\tau)$, of particle concentration fluctuations *versus* the logarithm of the delay time τ, measured at an angle (80°) near the position of the main peak of the static structure factor. Except for the equilibrium fluid phase at freezing ($\phi_f = 0.494$), measurements were made on the metastable fluid phases shortly after tumbling the samples but well before any crystals were evident.

ordered regions of particles. Below ϕ_g these highly asymmetric and thermodynamically unstable (due to their large surface to volume ratios) shear-induced nuclei dissipate by large-scale particle diffusion. Above ϕ_g, however, where dynamic light scattering indicates that large-scale diffusion is precluded, these structures remain frozen in the arrested metastable fluid. Particles adjacent to these shear-induced structures arrange themselves into registration through small-scale collective motions. This, in turn, provides additional free volume to the neighbouring particles aiding further growth of the plate-shaped crystals (Fig. 1) in the two most concentrated suspensions. This conjecture is given further support by the observation that the shape, orientation and growth rates of the crystals that develop in the kinetically arrested glass depend on the shear history; the vertically aligned needle-shaped crystals seen in the last two photographs in Fig. 1 developed within minutes of commencing a regular small-amplitude rocking motion.

As random close packing is approached, and even the smallest scale motions are gradually arrested[6], undisturbed suspensions remain amorphous apart from some epitaxial crystal growth from the meniscus (see Fig. 1 of ref. 1). This growth is presumably aided by slow gravitational settling of the particles and registered on the shear-induced structures formed as the colloidal fluid drains down the walls of the cuvette after tumbling. One could further speculate that if formation of these shear-induced structures was prevented, by employing an alternative means of 'melting' or quenching at concentrations above ϕ_g, then the amorphous structure would persist indefinitely. □

Received 16 November 1992; accepted 1 March 1993.

1. Pusey, P. N. & van Megen, W. *Nature* **320,** 340-342 (1986).
2. Pusey, P. N. in *Liquids, Freezing and the Glass Transition* (eds Hansen, J. P., Levesque, D. & Zinn-Justin, J. (North-Holland, Amsterdam, 1991).
3. Aastuen, D. J. W., Clark, N. A., Cotter, L. K. & Ackerson, B. J. *Phys. Rev. Lett.* **57,** 1733-1736 (1986).
4. Schätzel, K. & Ackerson, B. J. *Phys. Rev. Lett.*, **68,** 337-340 (1992).
5. van Megen, W. & Pusey, P. N. *Phys. Rev.* A**43,** 5429-5441 (1991).
6. van Megen, W. & Underwood, S. M. *Phys. Rev.* E**47,** 248-261 (1993).
7. Paulin, S. E. & Ackerson, B. J. *Phys. Rev. Lett.* **64,** 2663-2666 (1980).
8. Hoover, W. G. & Ree, F. H. *J. chem. Phys.* **49,** 3609-3617 (1986).
9. Ackerson, B. J. *J. Rheol.* **34,** 553-590 (1990).

ACKNOWLEDGEMENTS. We thank B. Ackerson, A. Moodie and P. Pusey for discussions and P. Francis for technical assistance. Financial support for this work was provided by the Australian Research Council.

Scaling of the critical slip distance for seismic faulting with shear strain in fault zones

Chris Marone* & Brian Kilgore†

* Department of Earth, Atmospheric, and Planetary Sciences, Massachusetts Institute of Technology, Cambridge, Massachusetts, 02139, USA
† United States Geological Survey, Menlo Park, California 94025, USA

THEORETICAL and experimentally based laws for seismic faulting contain a critical slip distance[1–5], D_c, which is the slip over which strength breaks down during earthquake nucleation. On an earthquake-generating fault, this distance plays a key role in determining the rupture nucleation dimension[6], the amount of premonitory and post-seismic slip[7–10], and the maximum seismic ground acceleration[1,11]. In laboratory friction experiments, D_c has been related to the size of surface contact junctions[2,5,12]; thus, the discrepancy between laboratory measurements of D_c ($\sim 10^{-5}$ m) and values obtained from modelling earthquakes ($\sim 10^{-2}$ m) has been attributed to differences in roughness between laboratory surfaces and natural faults[5]. This interpretation predicts a dependence of D_c on the particle size of fault gouge[2] (breccia and wear material) but not on shear strain. Here we present experimental results showing that D_c scales with shear strain in simulated fault gouge. Our data suggest a new physical interpretation for the critical slip distance, in which D_c is controlled by the thickness of the zone of localized shear strain. As gouge zones of mature faults are commonly 10^2–10^3 m thick[13–17], whereas laboratory gouge layers are 1–10 mm thick, our data offer an alternative interpretation of the discrepancy between laboratory and field-based estimates of D_c.

We carried out experiments in a double-direct-shear testing apparatus (see ref. 18 for a description) in which two faults slide simultaneously (Fig. 1). We used quartz sand to simulate granular fault gouge and varied the initial layer thickness and particle size to assess their effect on D_c. Normal stress on the sliding surfaces was held constant at 25 MPa using a high-speed servocontroller and normal displacement was measured continuously to yield a record of gouge layer thickness during slip. To simulate the extreme roughness of natural fault surfaces, we sheared gouge between steel forcing blocks with grooves perpendicular to the sliding direction. This forces shear to occur within the layers and not at the layer boundaries[19]. A few trial tests and existing data[19] indicate that the frictional behaviour and constitutive parameters determined from these experiments are the same as for experiments in which fault gouge is sheared between rocks of equivalent roughness.

The general friction characteristics and layer thickness changes observed were similar to those reported by previous workers[2,20] (Fig. 1). Rapid compaction and strain hardening are followed by a transition to roughly linear layer thinning and shearing with constant coefficient of friction. The transition distance (~4 mm in Fig. 1) varies directly with layer thickness and initial gouge particle size. To investigate the constitutive properties of the gouge zone we imposed step changes in the remote slip velocity (between 1 and 10 $\mu m\,s^{-1}$), producing changes in friction and in the rate of compaction with displacement (Fig. 1). For an increase in slip rate the coefficient of friction increases and the layer dilates, and for a decrease in slip rate, friction decreases and the layer compacts. Both friction and the rate at which layer thickness changes with displacement evolve following a change in slip rate (Fig. 1).

The parameter D_c is the characteristic distance of the exponential decay following the immediate friction change (Fig. 1). Because of the finite stiffness of the experimental apparatus, D_c must be obtained by modelling. We used a one-degree-of-

freedom spring-slider model to describe elastic interaction between the gouge layer and testing machine. This relation was coupled to a rate and single-state-variable constitutive law[2,3], and D_c was obtained from an iterative, least-squares inversion scheme[21]. A single-state-variable law typically simulates the data well, matching both the magnitude of the immediate friction change and the subsequent evolution. Details of the modelling and the other constitutive parameters will be reported elsewhere (C.M., manuscript in preparation). D_c values were obtained for 12 experiments using three layer thicknesses (0.7 mm, 2.1 mm and 4.2 mm) and three initial particle size distributions (fine, fractal and coarse; see Fig. 2 for details). Because of the large number of data points, only D_c values for velocity decreases are plotted (Fig. 2); velocity increases show the same trends.

The data for D_c against layer thickness (inset to Fig. 2) show two main features. First, in agreement with previous work[2,20], D_c scales directly with initial particle size, and for a given initial layer thickness and particle size, D_c decreases systematically with displacement and layer thinning. The rate of D_c reduction with thinning varies inversely with initial layer thickness and is roughly independent of initial particle size (inset to Fig. 2). Second, D_c is not in general a unique function of layer thickness. However, for a given displacement (lines in Fig. 2 inset) D_c scales roughly linearly with thickness at a rate of ~6 to 10 $\mu m\ mm^{-1}$. This trend is lower than the trend of D_c against thickness for a given experiment, which ranges from about 21 to 43 $\mu m\ mm^{-1}$, depending on initial thickness.

Differences in the D_c-thickness trends can be reconciled if we account for differences in shear strain between experiments (Fig. 2). Shear strain is calculated as $\int du/h$, where u is shear displacement and h is layer thickness. The data show that D_c decreases systematically and nonlinearly with shear strain and that initially coarse particles yield the largest D_c values for all strains.

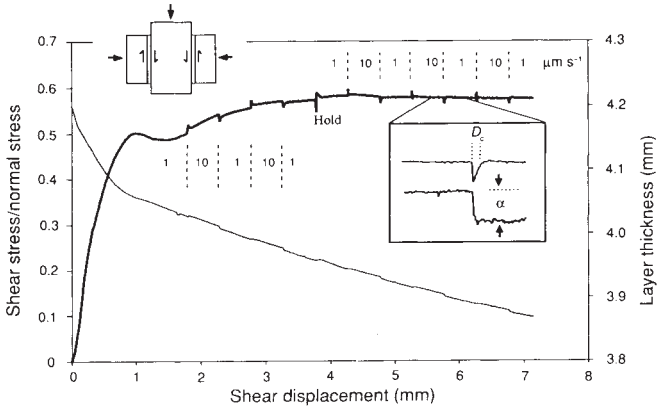

FIG. 1 Upper inset shows double-direct-shear configuration in which two gouge layers (stippled regions) are sheared simultaneously. Main plot shows normalized shear stress (bold curve) and layer thickness (of one layer) for fine quartz gouge. Beginning at ~2.0 mm displacement, the remote slip rate was cycled between 1.0 and 10.0 $\mu m\ s^{-1}$. Inset shows enlargement of friction data (upper curve) and detrended layer thickness (a linear trend was removed from the thickness data). D_c is the evolution distance of friction following a change in remote slip rate. It represents a memory of friction for the past state of the slipping region, in this case a state produced by slip at a given velocity. Although D_c is obtained by modelling, it is possible to see directly from the data (main plot) that D_c decreases with displacement. The parameter α is the change in thickness due to the change in slip velocity. For granular fault gouge α is positive for an increase in velocity, representing dilation of the gouge layer[19]. Shear displacement has been corrected for elastic distortion of the experimental apparatus and layer thickness has been corrected for thinning which occurs as the gouge layer is offset[20]. The gouge layer compacts during initial shear (up to ~1 mm) but subsequent thinning is due almost entirely to geometric thinning and localized strain along oblique Riedel shears[31]. 'Hold' denotes a point at which shear was momentarily (2 to 5 minutes) stopped while the control displacement transducer and data logger were reset. Data were collected every 0.25 μm of shear displacement.

The reduction in D_c with shear strain could in principle be caused by comminution, given the particle-size dependence of D_c. But the average particle size for coarse gouge after shear is 50–100 μm, whereas the ultra-fine particles start at 1–10 μm. As D_c is larger for thick ultra-fine gouge than for thin coarse gouge (Fig. 2), the D_c reduction with strain cannot be a simple comminution effect. Furthermore, because coarse particles have a very narrow initial size range, and hence more open packing than the fractal and ultra-fine particles, one expects a higher comminution rate for the coarse particles and hence a larger change in D_c with strain. Instead, the change in D_c with shear strain is roughly independent of initial particle size distribution (Fig. 2). The change therefore cannot be explained by comminution.

The steeper D_c-thickness trend in a given experiment compared with that for a given displacement (Fig. 2 inset) implies that in an experiment D_c decreases because of layer thinning and a displacement effect such as comminution or strain localization. As argued above, if comminution were responsible we would expect the D_c-thickness relation for a given experiment to scale strongly with particle size, which it does not. On the other hand, if we assume that strain localizes with displacement, then the reduction in D_c during an experiment could reflect a progressive narrowing of the region over which strain is accommodated and processes controlling D_c operate. This interpretation is consistent with the form of the D_c-strain data, which, in agreement with theory and experimental evidence[22,23], would imply nonlinear thinning of the localized zone ('shear band').

Although we cannot directly measure shear band thickness, we assume that dilatancy and volumetric strain within the region accommodating shear provide an indirect measure of the volume of that region and, hence, shear band thickness[24]. We define the parameter $\alpha = \Delta h / \Delta \log V$ (Fig. 1) as the change in layer thickness h on a change in slip velocity V (Fig. 3). α scales with particle size and shows a strong, positive correlation with D_c (inset to Fig. 3). Following the above discussion for D_c, the decrease of α with shear strain cannot be interpreted as a comminution effect, as it is roughly independent of particle size. Furthermore, comminution and subsequent tighter packing of the gouge particles should result in progressively larger dilation, and hence larger α, with shear for a given material volume, contrary to the observed trend (Fig. 3). On the other hand, under the assumption that the dilation (or compaction) magnitude scales with the volume of material participating in shear, the data of Fig. 3 imply progressive narrowing of the zone of strain accommodation. Together with the relation between D_c and α, this implies that the micromechanical processes controlling D_c operate within a zone of finite thickness, which narrows with increasing strain.

We offer the following physical interpretation for the relation between D_c and shear band thickness. For a shear band of thickness T and average grain diameter d, slip is distributed over $n = T/d$ particle-particle contacts. On a change in slip velocity at the shear zone boundary, each contact evolves with characteristic distance d_c and the shear band as a whole has $D_c = n d_c \chi$, where χ is a geometric factor to account for contact orientation. The parameter d_c is the characteristic friction distance for a single interface, which for bare rock surfaces is ~1 μm (refs 2, 21). This can be related to grain diameter, d, as $d_c = d\zeta$, where ζ is a constant to account for the ratio of contact junction size to grain diameter and the displacement needed for sliding to develop fully at a contact[25]. Combining these relations and the constants gives $D_c = nd\gamma = T\gamma$, which predicts a linear dependence of D_c on shear band thickness.

We may estimate the factor γ from our experiments if we

assume that under small strains shear is pervasive. The shear band then corresponds to the entire gouge thickness. As the minimum strain for localized shear is expected to increase with initial particle size[20,26], this assumption is most reasonable for small displacements and thick coarse gouge, for which D_c = 31 μm and T = 3.2 mm (Fig. 2), yielding $\gamma \approx 0.01$. We can use our scaling relation to estimate D_c for natural faults by noting that recent work (ref. 15) indicates that most slip on mature faults occurs within the fault-zone core, in an ultracataclasite zone which corresponds to the zone of active shear. For an exhumed section of the southern San Andreas fault system, the thickness of the ultracataclasite zone is T = 10 cm (ref. 15), which from our scaling relation yields D_c = 1 mm. This is in reasonable agreement with field and modelling estimates, which range from 0.1 mm (ref. 27) to ~1 cm (refs 1, 5–8, 29).

D_c has generally been interpreted in terms of the mechanics of contact junctions on surfaces free of gouge[2,5]. Here, we have shown instead that D_c depends on the thickness of gouge that participates in shear. Our physical model, in which D_c for a shear band derives from d_c for the constituent particle–particle contacts, provides a mechanism for linking friction of fault gouge with friction of bare rock surfaces, and a means of generalizing the results of detailed friction studies of bare rock surfaces.

Our data imply that D_c for natural faults will depend on the nature of gouge and strain accumulation. For a fault zone which accumulates strain without significant wear and gouge zone thickening, the trend of D_c with shear strain should resemble our experimental data (Fig. 2), yielding a critical slip distance

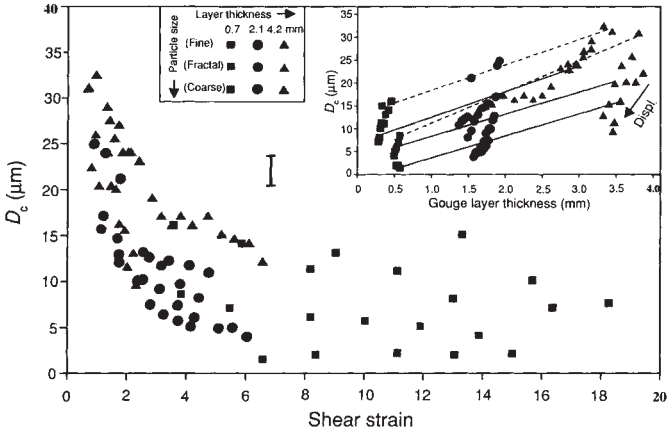

FIG. 2 D_c values from 12 experiments plotted against layer thickness (inset) and shear strain. Symbol colour and shape denote different initial particle sizes and layer thicknesses. Main plot: for a given initial particle size, D_c decreases systematically with shear strain. Inset: arrow shows increasing displacement during a given experiment. Several D_c values are obtained from each experiment, and layers thin with slip (for example, the red triangles are obtained from a single experiment, such as in Fig. 1). D_c is not a unique function of layer thickness, but lines connecting points of equal shear displacement indicate that for a given displacement and initial particle size D_c increases with thickness (dashed lines connect points for 2.3 mm displacement, solid lines connect 5.7 mm points). Error bar denotes resolution of D_c from modelling. Of the nine different initial configurations of particle size and layer thickness, we duplicated three sets (0.7-mm-thick coarse gouge; 2.1-mm ultra-fine gouge; and 4.2-mm coarse gouge) and checked several others with similar configurations (different normal stress, surface roughness or initial thickness). Experimental reproducibility was good. Starting gouge material: 'fine', commercially ground pure quartz powder, Silcosil 400 mesh, median and maximum diameter of 1.4 and 10 μm, respectively[30]; 'fractal', particle size distribution given by $N(n) = bn^{-D}$, where $N(n)$ is the number of particles of size n, b is a constant and D is the fractal dimension 2.6 (made, following ref. 20, by estimating the number of particles by weight and using size ranges from <45 to 710 μm); 'coarse' Ottawa sand, ASTM C-190; particle diameter 600–800 μm.

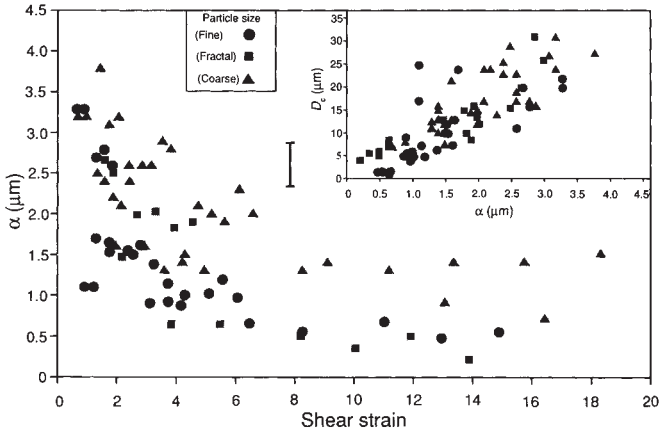

FIG. 3 Alpha is the change in layer thickness for a change in remote slip velocity (see inset to Fig. 1). Symbols denote different initial particle sizes. The data show a strong correlation with D_c (inset) and, within the resolution, a systematic variation with shear strain. Comparison with Fig. 2 indicates that α scales with shear strain and is independent of gouge thickness. Initially coarse particles yield the highest α for a given shear strain or displacement. We assume that α is a measure of the volume of gouge material participating in shear and hence the thickness over which strain is accommodated (shear band thickness). Thus, the relationship between α and D_c implies that D_c scales with shear band thickness. Error bar indicates measurement resolution.

independent of nominal gouge thickness. On the other hand, rapid gouge accumulation (via steady wear or inclusion of brecciated wall rock during earthquake rupture[28]) or re-working of an existing gouge zone would produce a thick, low-strain fault zone and thus large D_c. This suggests that mature faults with thick gouge zones may have significantly higher D_c than faults with negligible net slip or those which otherwise have little accumulated gouge.

As D_c is an evolution distance, representing a memory of friction for past states of the slipping region, our data imply that faults with thick ultracataclasite zones will require larger slip to effect a given change in friction. On an earthquake fault, this implies greater precursory slip before rupture nucleation, and in general, a greater tendency for stable sliding, because instability is enhanced by rapid changes in frictional resistance. Thus mature faults with thick gouge zones and large D_c may show greater preseismic slip and have larger nucleation zones than faults with negligible gouge zones. □

Received 16 November 1992; accepted 9 March 1993.

1. Ida, Y. *J. geophys. Res.* **77,** 3796–3805 (1972); *Bull. seism. Soc. Am.* **63,** 959–968 (1973).
2. Dieterich, J. H. *J. geophys. Res.* **84,** 2161–2168 (1979); in *Mechanical Behaviour of Crustal Rocks, Geophys. Monogr. Ser. Vol. 24* (eds Carter, N. L., Friedman, M., Logan, J. M. & Sterns, D. W.) 103–120 (Am. Geophys. Un., Washington DC, 1981).
3. Ruina, *J. geophys. Res.* **88,** 10359–10370 (1983).
4. Andrews, D. J. *Bull. seism. Soc. Am.* **75,** 1–21 (1985).
5. Scholz, C. H. *Nature* **336,** 761–763 (1988).
6. Dieterich, J. H. in *Earthquake Source Mechanics* (eds. Das, S., Boatwright, J. & Scholz, C.) 37–47 (Am. Geophys. Un., Washington DC, 1986); *Tectonophysics* **211,** 115–134 (1992).
7. Tse, S. T. & Rice, J. R. *J. geophys. Res.* **91,** 9452–9472 (1986).
8. Lorenzetti, E. & Tullis, T. E. *J. geophys. Res.* **94,** 12,343–12,361 (1989).
9. Marone, C., Scholz, C. H. & Bilham, R. *J. geophys. Res.* **96,** 8441–8452 (1991).
10. Stuart, W. D. *Pure appl. Geophys.* **126,** 619–641 (1988).
11. Aki, K. *J. geophys. Res.* **84,** 6140–6148 (1979); **92,** 1349–1355 (1987).
12. Rabinowicz, E. J. *J. appl. Phys.* **22,** 1373–1379 (1951); **27,** 131–135 (1956).
13. Feng, R. & McEvilly, T. V. *Bull. seism. Soc. Am.* **73,** 1701–1720 (1983).
14. Scholz, C. H. *Geology* **15,** 493–497 (1987).
15. Chester, F. M., Evans, J. P. & Biegel, R. L. *J. geophys. Res.* **98,** 771–786 (1993).
16. Michelini, A. & McEvilly, T. V. *Bull. seism. Soc. Am.* **81,** 524–552 (1991).
17. Montgomery, D. R. & Jones, D. L. *Geology* **20,** 55–58 (1992).
18. Linker, M. F. & Dieterich, J. H. *J. geophys. Res.* **97,** 4923–4940 (1992).
19. Marone, C., Raleigh, C. B. & Scholz, C. H. *J. geophys. Res.* **95,** 7007–7025 (1990).
20. Biegel, R. L., Sammis, C. G. & Dieterich, J. H. *J. struct. Geol.* **11,** 827–846 (1989).
21. Marone, C. & Cox, S. J. D. *Eos* **71,** 457 (1991).
22. Mühlaus, H.-B. & Vardoulakis, I. *Géotechnique* **37,** 271–283 (1987).
23. Jaeger, H. M. & Nagel, S. R. *Science* **255,** 1523–1532 (1992).
24. Lambe, T. W. & Whitman, R. V. *Soil Mechanics* (Wiley, New York, 1969).

25. Boitnott, G. N., Biegel, R. L., Scholz, C. H., Yoshioka, N. & Wang, W. *J. geophys. Res.* **97,** 8965–8978 (1992).
26. Marone, C. & Scholz, C. H. *J. struct. Geol.* **11,** 799–814 (1989).
27. Power, W. L. & Tullis, T. E. *J. geophys. Res.* **97,** 15425–15435 (1992).
28. Sibson, R. H. *Nature* **316,** 248–251 (1985); *Pure appl. Geophys.* **124,** 159–176 (1986).
29. Rice, J. R. *J. geophys. Res.* (in the press)
30. Wong, T.-F. & Zhao, Y. *Tectonophysics* **175,** 177–195 (1990).
31. Scott, D. R., Marone, C. & Sammis, C. *J. geophys. Res.* (submitted).

ACKNOWLEDGEMENTS. The experiments were done at the U.S. Geological Survey, Menlo Park. C.M. thanks J. Dieterich for making his laboratory available for the experiments and for encouragement. We thank R. Jeanloz, C. Scholz and C. Sammis for helpful comments and suggestions on the manuscript. This work was supported by the NSF.

Variations in mercury deposition to Antarctica over the past 34,000 years

Grace M. Vandal*, William F. Fitzgerald*, Claude F. Boutron†‡ & Jean-Pierre Candelone†

* Department of Marine Sciences, University of Connecticut, Avery Point, Groton, Connecticut 06340, USA
† Laboratoire de Glaciologie et Géophysique de l'Environnement du CNRS, 54 rue Molière, Domaine Universitaire, BP 96, 38402 St Martin d'Hères cedex, France
‡ UFR de Mécanique, Université Joseph Fourier de Grenoble, Domaine Universitaire, BP 68 38041 Grenoble, France

POLAR ice contains a valuable record of past atmospheric mercury deposition, which can provide information about both the natural biogeochemical cycling of this toxic trace metal and the impact of recent anthropogenic emissions. But existing studies of mercury in polar ice and snow cores[1–5] suffer from sample contamination and inadequate analytical procedures. Here we report measurements of mercury concentrations spanning the past 34,000 years from the Dome C ice core, Antarctica, using the stringent trace-metal clean protocols developed by Patterson and co-workers[6]. Although this record does not extend into the industrial period, it provides an important baseline for future attempts to identify anthropogenic mercury in Antarctic ice and snow. We find that mercury concentrations were strikingly elevated during the last glacial maximum (18,000 years ago), when oceanic productivity may have been higher than it is today[7]. As oceanic mercury emission is correlated with productivity[8,9], we suggest that this was the principal pre-industrial source of mercury to Antarctica; mercury concentrations in Antarctic ice might therefore serve as a palaeoproductivity indicator for the more distant past.

The historical record of mercury deposition contained in polar ice cores yields information on the natural biogeochemical mercury cycle and provides a way to assess the impact of modern anthropogenic emissions. The atmosphere is one main pathway for the distribution of mercury at the Earth's surface. For example, atmospheric mercury deposition greatly exceeds fluvial inputs to the oceans and is the principal input to many aquatic and terrestrial systems[10–12]. Gaseous elemental Hg (Hg^0) is the dominant atmospheric species and has a residence time of about a year. Elemental Hg is oxidized in the atmosphere and removed by wet or dry deposition. Atmospheric deposition contains principally ionic and particulate Hg species[11,12]. Modern human-related Hg emissions (coal combustion, waste incineration, smelting) to the atmosphere are comparable in magnitude to natural fluxes (oceanic emission, terrestrial biogenic volatiles, volcanoes)[11,13,14]. The effects on the natural Hg cycle are of concern because Hg and many of its compounds are toxic and can be converted to more poisonous forms (such as monomethyl mercury) in aquatic systems[15,16]. The surface waters of the equatorial Pacific Ocean are highly supersaturated with Hg^0 relative to atmospheric concentrations. Oceanic gas emission of Hg^0 is a principal source of Hg to the atmosphere and the magnitude of the efflux is related to productivity[8,9].

We have measured Hg in 14 sections of the Dome C core. Dome C is located in central Antarctica (77° 39′ S, 124° 10′ E) at an elevation of 3,240 m. The core is 905 m long and covers the past 40,000 years[17]. Details of the trace metal clean procedures and mechanical decontamination techniques used in the treatment of the Dome C core can be found in ref. 6. Briefly, the core sections were processed at the California Institute of Technology in the following manner. Each section was mechanically cleaned by chiselling four to six successive veneers of ice from the exterior towards the interior of the core section under ultra-clean conditions. The veneer layers were collected and analysed separately to determine the trace metal content of each section as a function of radius. The samples were acidified with ultra-pure HNO_3 to make a 0.1% HNO_3 solution. Aliquots for the determination of lead were removed and the remaining sample kept frozen except to thaw for the removal of a sample aliquot for analysis. Mercury was determined in aliquots of the 14 sections used for the determination of lead and other constituents. In addition to the ice-core samples, numerous blanks were included to assess Hg contributions from processing the core sections, acidification and storage in polyethylene bottles. Samples were shipped frozen to the University of Connecticut in April 1991 for Hg analysis.

Mercury concentrations in the sections of the Dome C core are listed in Table 1. Aluminium, sodium and non-sea-salt (n.s.s.) SO_4 are also reported in Table 1. Non-sea-salt SO_4 is the SO_4 concentration corrected for the sea-salt component and represents the product of the atmospheric oxidation of reduced sulphur species. The core covers four main climatic stages, as inferred from the oxygen isotope profile[17], and these are listed in chronological order: (1) the Holocene (0 to ~408 m depth), (2) the transition from the Last Ice Age to the Holocene (~408–548 m), (3) the Last Glacial Maximum (LGM; ~548–708 m)

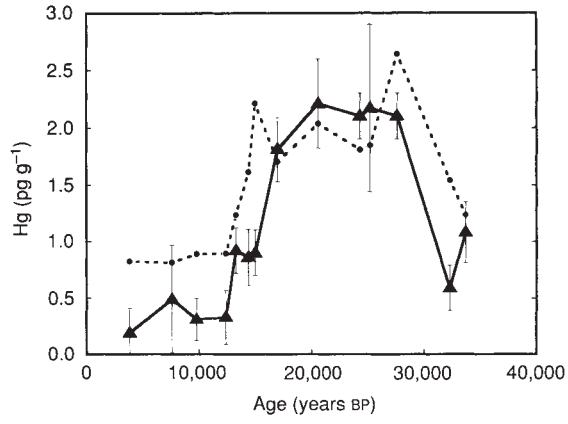

FIG. 1 *a*, (▲) Mercury distribution as a function of age in the Dome C ice core. The Hg concentration was less than 1.0 pg g^{-1} during the Last Ice Age, then increased to 2.1 pg g^{-1} during the LGM, remaining elevated for ~10,000 years before decreasing during the glacial to interglacial transition to ~0.4 pg g^{-1} in the Holocene. Mercury was determined in the ice and snow samples by $SnCl_2$ reduction and collection on gold-coated sand with gas-phase detection by cold vapour atomic fluorescence spectroscopy[22,29]. Analytical precision was generally ±5%. A blank of 0.16 pg Hg g^{-1} ice from the polyethylene sample bottles was detected and the measured Hg values corrected. Samples ranged from 3 to 40 g. The uncertainty in the reported concentrations associated with variations in analytical and storage blanks was ±0.2 pg g for a 20-g sample. *b*, (– · –) The predicted distribution of Hg in the Dome C ice core based on the marine-derived n.s.s. SO_4 concentrations and the estimated Hg/S ratio for gaseous oceanic evasion. The predicted and measured values are remarkably close, except in the Holocene where the estimate is greater than the measured values. The Hg/S ratio used is representative of a productive ocean region and the ratio of their emissions during the Holocene may be lower.